

Time-Reversal Symmetry Breaking Superconductivity in Three-Dimensional Dirac Semimetallic Silicides

Sudeep K. Ghosh,^{1,*} P. K. Biswas,^{2,†} Chunqiang Xu,^{3,4} B. Li,⁵ J. Z. Zhao,⁶ A. D. Hillier,^{2,‡} and Xiaofeng Xu^{3,§}

¹*School of Physical Sciences, University of Kent, Canterbury CT2 7NH, United Kingdom.*

²*ISIS Pulsed Neutron and Muon Source, STFC Rutherford Appleton Laboratory, Harwell Campus, Didcot, Oxfordshire OX11 0QX, United Kingdom.*

³*Key Laboratory of Quantum Precision Measurement of Zhejiang Province,*

Department of Applied Physics, Zhejiang University of Technology, Hangzhou 310023, China

⁴*School of Physics and Key Laboratory of MEMS of the Ministry of Education, Southeast University, Nanjing 211189, China*

⁵*Information Physics Research Center, Nanjing University of Posts and Telecommunications, Nanjing 210023, China*

⁶*Co-Innovation Center for New Energetic Materials, Southwest University of Science and Technology, Mianyang, China*

(Dated: February 3, 2022)

Superconductors with broken time-reversal symmetry represent arguably one of the most promising venues for realizing highly sought-after topological superconductivity that is vital to fault-tolerant quantum computation. Here, by using extensive muon-spin relaxation and rotation measurements, we report that the isostructural silicide superconductors (Ta, Nb)OsSi spontaneously break time-reversal symmetry at the superconducting transition while surprisingly showing a fully-gapped superconductivity characteristic of conventional superconductors. The first-principles calculations show that (Ta, Nb)OsSi are three-dimensional Dirac semimetals protected by nonsymmorphic symmetries. Taking advantage of the exceptional low symmetry crystal structure of these materials, we have performed detailed theoretical calculations to establish that the superconducting ground state for both (Ta, Nb)OsSi is most likely a nonunitary triplet state.

INTRODUCTION

Dirac or Weyl semimetals have attracted significant research interest due to their exceptional physical properties arising from the topologically protected gapless electronic excitations [1, 2]. Three-dimensional (3D) Dirac semimetals are particularly interesting because they can induce novel topological phases when symmetries are broken, e.g. a Dirac semimetal transforms into a Weyl semimetal with time-reversal symmetry (TRS) breaking [1]. However, research on topological semimetals to date has been primarily focused on characterizing the underlying nontrivial band topology, while their interplay with correlated electronic states, such as novel magnetism and unconventional superconductivity, remained largely an uncharted territory. On the other hand, an interesting class of unconventional superconductors includes the ones that spontaneously break TRS in the superconducting state [3] yet otherwise have properties similar to conventional BCS-type superconductors. As a result, superconducting 3D Dirac semimetals that break TRS in the superconducting state represent a unique class of materials to realize novel topological superconductivity [4] but are extremely rare.

A superconducting order parameter which breaks TRS is, generically, required to have multiple components with non-trivial phases in between [3]. Such a multi-component order parameter arises from a multidimensional irreducible representation [5, 6] of the crystal point group of the material. However, it is usually difficult to unambiguously establish the structure of the super-

conducting order parameters for the TRS-breaking superconductors mainly due to two reasons: a) lack of sufficient knowledge of the electron pairing mechanism and b) highly symmetric crystal structures leading to many possibilities with similar low-temperature properties. This limits our ability to work by the process of elimination. For example, the point group D_{4h} of Sr_2RuO_4 allows for 20 possibilities with weak spin-orbit coupling (SOC) and 2 possibilities with strong SOC, of TRS-breaking superconducting instabilities [5, 6]. In this regard, the superconductors LaNiC_2 [7, 8], LaNiGa_2 [9–12] and UTe_2 [13] are exceptions due to their very low-symmetry crystal structure that leads only to a few symmetry-allowed superconducting order parameters. In contrast to LaNiC_2 [8] and LaNiGa_2 [10, 11], which show two full gaps, UTe_2 shows nodal behaviour [14] in their respective TRS-breaking superconducting state.

The recently discovered Osmium-based silicide superconductors (Ta,Nb)OsSi [15] have a very low-symmetry crystal structure as well and weak electron-phonon coupling [16]. In this article, by a combination of multiple experimental techniques including muon-spin rotation and relaxation (μSR) and thermodynamic measurements along with a detailed theoretical analysis, we demonstrate that (Ta,Nb)OsSi belong to nonsymmorphic symmetry-protected 3D Dirac semimetals that spontaneously break TRS at the superconducting transition but behave as conventional superconductors otherwise. By means of symmetry analysis and model calculations, our observations are found to be consistent with a nonunitary triplet superconducting ground state, the verification of which shall stimulate further study, both experimentally

and theoretically.

RESULTS AND DISCUSSION

(Ta, Nb)OsSi crystallize in a TiNiSi-type centrosymmetric orthorhombic crystal structure and have similar physical and chemical properties [15]. We prepared polycrystalline samples of (Ta, Nb)OsSi using conventional solid state reaction method and systematically investigated their physical properties using detailed μ SR measurements in zero-field (ZF), longitudinal-field (LF) and transverse-field (TF) modes; magnetic-susceptibility, specific-heat and electrical-resistivity measurements [17]. The μ SR measurements were performed using the MUSR spectrometer at the ISIS Pulsed Neutron and Muon Source, UK. The temperature dependence of the magnetic susceptibility, collected in zero-field-cooled mode on the same samples, is shown by the solid blue lines on the right axis of Fig. 1b (Fig. 1d) for TaOsSi (NbOsSi). It indicates bulk superconductivity with $T_c \approx 5.5$ K in TaOsSi and $T_c \approx 3.1$ K in NbOsSi.

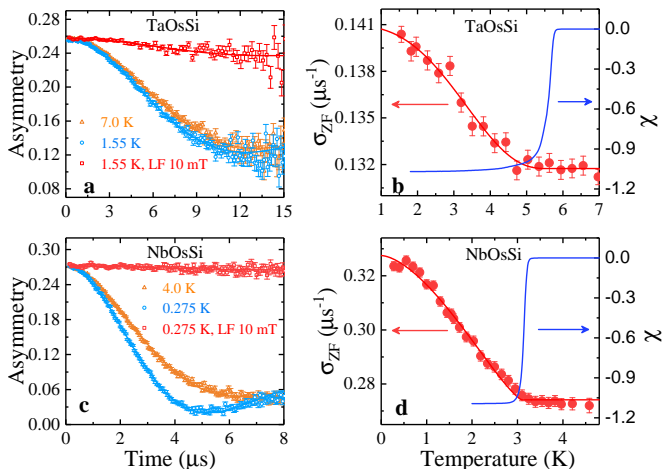


FIG. 1. Time-reversal symmetry breaking observed in (Ta, Nb)OsSi by ZF- μ SR measurements. **a** and **c**: ZF- μ SR time spectra collected above and below T_c for TaOsSi and NbOsSi respectively. The solid lines are the fits to the data using Eq. 1. **b** and **d**: The temperature dependence of the muon spin relaxation rate σ_{ZF} of TaOsSi and NbOsSi respectively. Both show a clear systematic increase in σ_{ZF} just below T_c . The corresponding T_c -s are shown in the diamagnetic shifts in the magnetic susceptibility data of the two materials by the solid blue lines. The error bars shown are the standard deviations in the respective measurements.

ZF- μ SR: ZF- μ SR measurements were performed in search for spontaneous magnetic fields that can appear in the superconducting state leading to breaking of TRS. Fig. 1a and Fig. 1c show the ZF- μ SR time spectra for TaOsSi and NbOsSi respectively, collected above and be-

low the respective T_c -s. A clear increase in the muon-spin relaxation rate in the superconducting state compared to the normal state is evident from both figures. The ZF- μ SR time spectra over a range of temperatures across the T_c for both materials were collected. The data were fitted using a Gaussian Kubo-Toyabe relaxation function [18] $\mathcal{G}(t) = \frac{1}{3} + \frac{2}{3}(1 - \sigma_{ZF}^2 t^2) \exp(-\sigma_{ZF}^2 t^2/2)$ multiplied by an exponential decay giving rise to the asymmetry function

$$A(t) = A(0)\mathcal{G}(t)\exp(-\lambda_{ZF}t) + A_{bg}. \quad (1)$$

$A(0)$ and A_{bg} are the initial and background asymmetries of the ZF- μ SR time spectra. σ_{ZF} and λ_{ZF} represent the muon spin relaxation rates originating from the presence of nuclear and electronic moments in the sample, respectively. In the fitting process, the electronic relaxation rate λ_{ZF} was found to be nearly temperature independent for both materials with small average values of $0.0243(2) \mu\text{s}^{-1}$ for TaOsSi and $0.0633(5) \mu\text{s}^{-1}$ for NbOsSi and hence was kept fixed. This indicates the absence of fast-fluctuating electronic moments. The nuclear relaxation rate $\sigma_{ZF}(T)$ shown in Fig. 1b (Fig. 1d) for TaOsSi (NbOsSi), on the other hand, shows a clear systematic increase just below T_c . The LF- μ SR measurements performed under a field-cooled condition with a small field of 10 mT shown in Figs. 1a and 1c clearly rule out the possibility of defect- or impurity-induced relaxations since the small field is enough to decouple the muon spins from the weak relaxation channels in both samples. This demonstrates that the increase in σ_{ZF} just below T_c is due to very weak fields which are static or quasi-static on the time-scale of muon life-time and are closely tied to the superconducting state, providing conclusive evidence of spontaneously broken TRS in the superconducting ground states of (Ta,Nb)OsSi. The spontaneous field estimated from the change $\Delta\sigma_{ZF} = \sigma_{ZF}(T \approx 0) - \sigma_{ZF}(T > T_c)$ is $B_{int} \approx \sqrt{2}\Delta\sigma_{ZF}/\gamma_\mu = 0.17$ G (0.83 G) for TaOsSi (NbOsSi) which is similar to other TRS breaking superconductors [3]. Here, $\gamma_\mu = 2\pi \times 135.5$ MHz/T is the muon gyromagnetic ratio [19].

TF- μ SR: To determine the superconducting gap symmetry of (Ta,Nb)OsSi, we have performed extensive TF- μ SR measurements in a transverse field of 30 mT applied above T_c and cooled to the base temperature to stabilize a well-ordered flux-line-lattice in the mixed state of the superconductors. The TF- μ SR asymmetry signals collected above and below T_c are shown in Fig. 2a (Fig. 2d) for TaOsSi (NbOsSi). For both materials, the asymmetry signals above T_c show very little relaxation due to the transverse component of weak nuclear moments present in these materials, while those below T_c show higher relaxation due to the added inhomogeneous field distribution of the flux-line-lattice. The TF- μ SR asymmetry signals were analysed using a Gaussian damped sinusoidal function plus a non-decaying oscillation that contributes

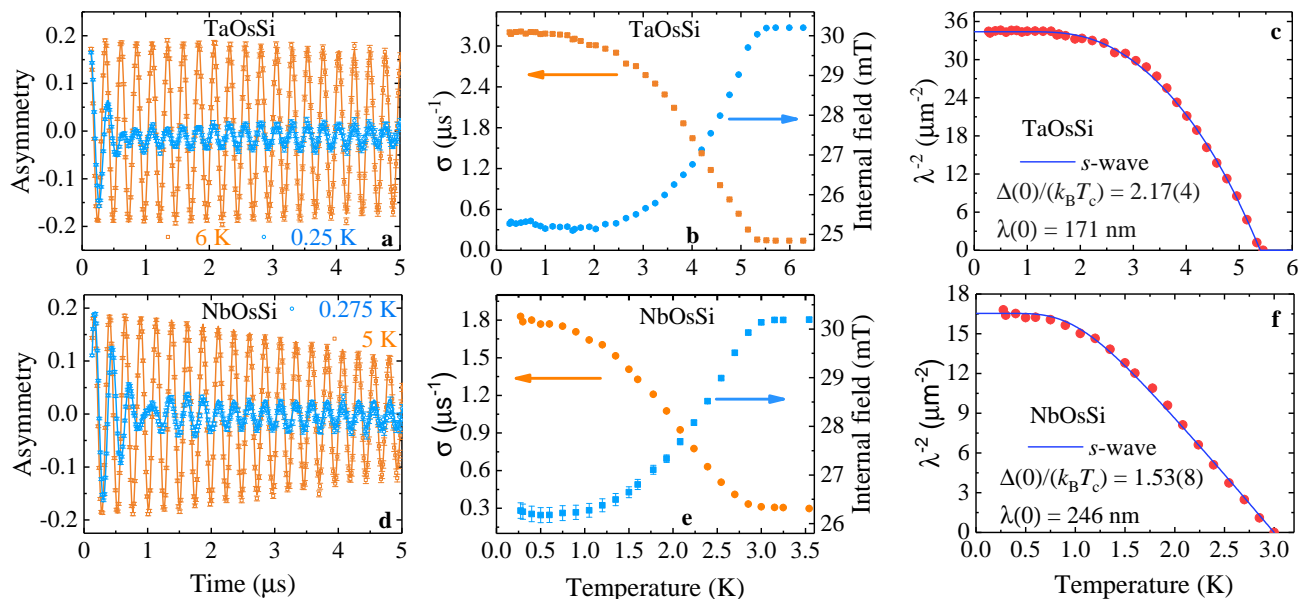


FIG. 2. **Characterizing the superconducting properties of (Ta, Nb)OsSi by TF- μ SR measurements.** **a** and **d**: TF- μ SR time spectra, collected above (red square) and below (blue circle) the T_c in a field-cooled transverse field of 30 mT for TaOsSi and NbOsSi respectively. The solid lines are the fits to the data using Eq. 2. **b** and **e**: The temperature dependence of the extracted relaxation rate σ (left axis) and internal field (right axis) for TaOsSi and NbOsSi respectively. **c** and **f**: The temperature dependence of the inverse magnetic penetration depth squared or equivalently the superfluid density $\rho_s \propto \lambda^{-2}(T)$ for TaOsSi and NbOsSi respectively. The solid lines are fits to the data with an isotropic single-gap s -wave model.

to the muons stopping in the silver sample holder:

$$A_{TF}(t) = A(0) \exp(-\sigma^2 t^2 / 2) \cos(\gamma_\mu \langle B \rangle t + \phi) + A_{bg} \cos(\gamma_\mu B_{bg} t + \phi). \quad (2)$$

Here $A(0)$ and A_{bg} are the initial sample and background asymmetries respectively, $\langle B \rangle$ and B_{bg} are the average internal and background magnetic fields respectively, ϕ is the shared phase offset and σ is the depolarization rate of the muon spin precession signal originating from the variance of the magnetic-field distribution in the superconductor. Fig. 2**b** and Fig. 2**e** show the temperature dependence of the relaxation rate σ (left axis) and internal field (right axis) of TaOsSi and NbOsSi respectively, extracted from the fits to the asymmetry signals using Eq. 2. The internal fields at the muon sites show strong diamagnetic shifts below T_c for both materials, a clear indication of bulk superconductivity. The $\sigma = (\sigma_{sc}^2 + \sigma_{nm}^2)^{1/2}$ includes contributions from both the flux-line-lattice σ_{sc} and a temperature-independent relaxation due to nuclear moments $\sigma_{nm} = 0.146 \mu s^{-1}$ ($0.312 \mu s^{-1}$) for TaOsSi (NbOsSi), determined from the average values of σ collected above the respective T_c -s where it is mostly temperature independent.

The London magnetic penetration depth λ can be computed from σ_{sc} within a Ginzburg-Landau treatment of the vortex state in a superconductor in the limit of the

applied field $H \ll H_{c2}$ [20] as:

$$\frac{\sigma_{sc}(T)}{\gamma_\mu} = 0.06091 \frac{\Phi_0}{\lambda^2(T)}, \quad (3)$$

where $\Phi_0 = 2.068 \times 10^{-15}$ Wb is the flux quantum. The temperature dependence of λ^{-2} extracted using the above equation for TaOsSi and NbOsSi are presented in Fig. 2**c** and Fig. 2**f** respectively. Since $\lambda^{-2}(T)$ is a measure of the superfluid density $\rho_s \propto \lambda^{-2} \propto n_s/m^*$ (n_s is the charge carrier concentration, and m^* is the effective mass of the charge carriers), it bears signatures of the symmetry of the superconducting gap. We note from Fig. 2**b** and Fig. 2**e** that the superfluid density of both materials shows saturation below $T_c/3$ which indicates the absence of low-lying excited states close to zero temperature, a hallmark of node-less superconductivity.

To understand the superconducting pairing symmetry, we analyse the temperature dependence of the superfluid density within the local London approximation ($\lambda(0) \gg \xi$, ξ is the coherence length) [21] by:

$$\frac{\lambda^{-2}(T)}{\lambda^{-2}(0)} = 1 + 2 \left\langle \int_{\Delta_{\mathbf{k}}(T)}^{\infty} \left(\frac{\partial f}{\partial E} \right) \frac{E dE}{\sqrt{E^2 - |\Delta_{\mathbf{k}}(T)|^2}} \right\rangle_{FS}. \quad (4)$$

Here, $\Delta_{\mathbf{k}}(T)$ is the form of the gap function for a given pairing model, $f(E, T) = [1 + \exp(E/k_B T)]^{-1}$ is the Fermi function and $\langle \rangle_{FS}$ represents an average over a spherical Fermi surface. For an isotropic single gap s -

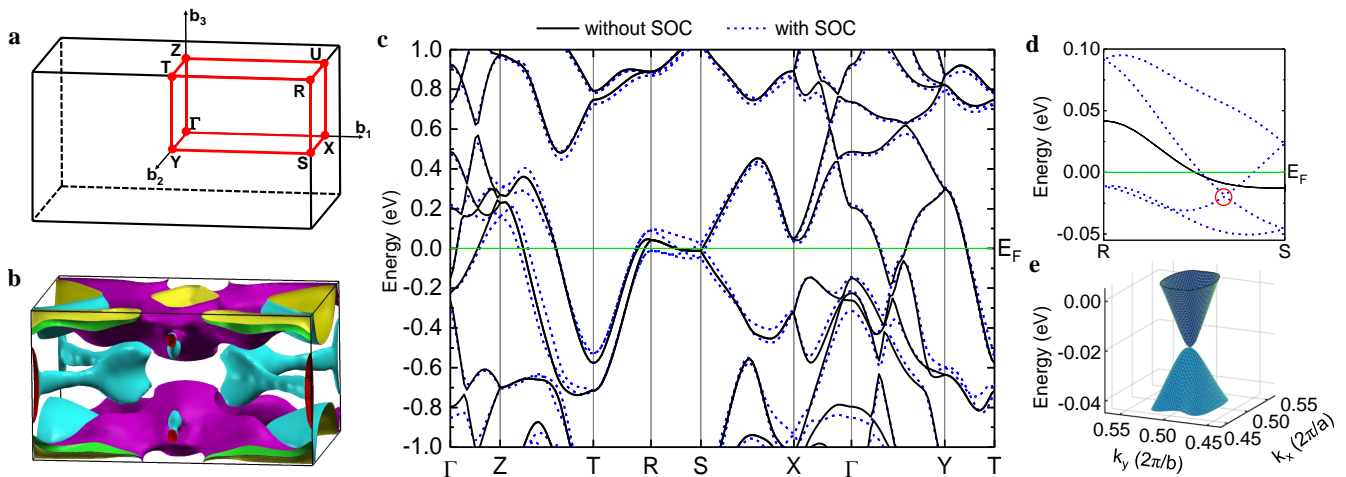


FIG. 3. **Band structure of NbOsSi.** **a)** First Brillouin zone with the high symmetry points marked. **b)** Combined view of all the four Fermi surface sheets of NbOsSi without SOC. The large parallel sections of the Fermi surface sheets are clearly visible. **c)** The band structure of NbOsSi with and without considering SOC. **d)** Enlarged view of the band structure along the RS-direction. The Dirac point is marked by the red circle. **e)** The dispersion close to the Dirac point marked in **d**.

wave model, $\Delta_{\mathbf{k}}(T)$ is independent of \mathbf{k} and its temperature dependence is given by [22]

$$\Delta(T) = \Delta(0) \tanh \left[1.82 \{1.018 (T_c/T - 1)\}^{0.51} \right]. \quad (5)$$

The solid lines in the Fig. 2c and Fig. 2f show that the superfluid density can be fitted quite well with an isotropic single-gap *s*-wave model both for TaOsSi and NbOsSi respectively. We note that the values of the fitting parameter $\frac{\Delta(0)}{k_B T_c}$ for both (Ta,Nb)OsSi are close to its weak-coupling BCS limit value.

Band structure and specific heat: The space group of (Ta,Nb)OsSi is Pnma (no. 62) and the point group is D_{2h} . The first Brillouin zone with the high-symmetry directions marked is shown in Fig. 3a. Pnma is a nonsymmorphic space group having three glide planes: $G_1 = \{m_{(0,1,0)}|t_{(0,1/2,0)}\}$, $G_2 = \{m_{(0,0,1)}|t_{(1/2,0,1/2)}\}$ and $G_3 = \{m_{(1,0,0)}|t_{(1/2,1/2,1/2)}\}$ where *m* and *t* denote the mirror plane and fractional translation parallel to the plane respectively. Two-fold degeneracies along the high symmetry lines *XS*, *XU*, *UR* and *RS* result from G_2 and that along *YS* and *UZ* result from G_3 [17]. The band structure of NbOsSi (which is similar to that of TaOsSi [16, 23]) computed using density functional theory within the generalized gradient approximation is shown in Fig. 3c with and without the effect of SOC. We note that SOC leads to small yet finite splitting of the bands near the Fermi level with a maximum splitting ~ 100 meV near the *R* point (maximum splitting ~ 140 meV near the *S* point for TaOsSi [23]).

(Ta, Nb)OsSi are inherently multi-band systems with the Nb 4*d*-orbitals (Ta 5*d*-orbitals) and the Os 5*d*-orbitals contributing the most to the density of states

(DOS) at the Fermi level. There are four Fermi surface sheets (without SOC) with two of them contributing $\sim 80\%$ to the DOS at the Fermi level [17]. A combined view of all the four Fermi surface sheets of NbOsSi without SOC is shown in Fig. 3b.

The Kramer's theorem guarantees that all the electronic bands of non-magnetic centrosymmetric materials (Ta,Nb)OsSi are at least two-fold degenerate even in the presence of SOC. We find that (Ta,Nb)OsSi have four bulk Dirac points within $\sim 10 - 20$ meV energy window below the Fermi level [17]. Two of these Dirac points lie on the *RS* \bar{R} -line ($\bar{R} \equiv -R$) and are protected by the nonsymmorphic symmetry G_2 which leads to the additional two-fold degeneracy. A zoomed-in view of the band structure of NbOsSi along the *RS* direction is shown in Fig. 3d and the dispersion close to the Dirac point along this line is shown in Fig. 3e. The other two Dirac points are, however, not protected by symmetry and the surface Fermi arcs are unfortunately not clearly distinguishable [17]. Thus (Ta,Nb)OsSi are nonsymmorphic symmetry-protected Dirac semimetals expected to have characteristic spectroscopic and transport properties [2].

As a result of the exceptionally low symmetry crystal structure of (Ta, Nb)OsSi, in the strong SOC limit, there are no symmetry allowed TRS breaking superconducting order parameters. In the weak SOC limit, while the relevant point group $D_{2h} \otimes SO(3)$ ($SO(3)$ is the group of spin rotations in three dimensions) has four symmetry allowed TRS breaking superconducting instabilities, all of them have nodes [9]. Thus clearly all the symmetry-allowed superconducting instabilities of (Ta, Nb)OsSi in the effective single band picture [24] are inconsistent with the experimental observations.

Motivated by the multi-band nature of (Ta, Nb)OsSi,

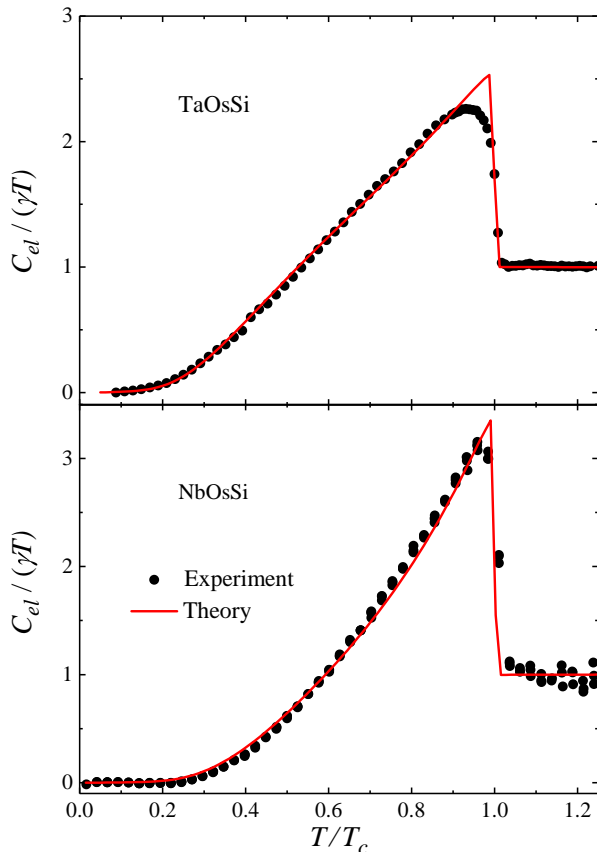


FIG. 4. **Electronic specific heat.** Temperature dependence of the experimentally measured electronic specific heat fitted with the theoretically computed specific heat in the INT state for the toy model with parameters $s/t = 0.1$, $\mu/t = -3.0$ and $\boldsymbol{\eta} = \frac{1}{\sqrt{3}}(1, e^{i\pi/100}, e^{i101\pi/100})$. The fitting parameters for TaOsSi case are $\Delta_0/(k_B T_c) = 2.20$ and $\alpha/t = 0.15$; and for NbOsSi case are $\Delta_0/(k_B T_c) = 2.63$ and $\alpha/t = 0.20$.

we consider an internally antisymmetric nonunitary triplet (INT) superconducting state [11] proposed in the case of LaNiGa₂, which has the same point group as (Ta, Nb)OsSi. Pairing in the INT state occurs between electrons on the same site but in two different orbitals in the nonunitary triplet channel and fermionic antisymmetry comes from orbital space. The pairing potential is $\hat{\Delta} = \hat{\Delta}_S \otimes \hat{\Delta}_B$ where the pairing potential in spin space is $\hat{\Delta}_S = (\mathbf{d} \cdot \boldsymbol{\sigma}) i \sigma_y$ and in orbital space is $\hat{\Delta}_B = i \tau_y$, with $\boldsymbol{\sigma}$ ($\boldsymbol{\tau}$) being the vector of Pauli matrices in spin space (orbital space). The triplet pairing is characterized by the \mathbf{d} -vector: $\mathbf{d} = \Delta_a \boldsymbol{\eta}$ with $|\boldsymbol{\eta}|^2 = 1$ which is nonunitary and is characterized by the real vector $\mathbf{q} = i(\boldsymbol{\eta} \times \boldsymbol{\eta}^*) \neq 0$, and Δ_a is the pairing amplitude considered to be uniform to realize an isotropic gap observed in (Ta, Nb)OsSi.

There are several extended regions inside the Brillouin zone of (Ta, Nb)OsSi where two of the Fermi surface sheets are parallel and close to each other as shown in Fig. 3b for example. This feature is essential to stabilize

the INT state and we model it by considering a simple toy model with two bands $\epsilon_{\pm}(\mathbf{k}) = \epsilon(\mathbf{k}) \pm s$ emerging from two nearly degenerate effective orbitals rigidly shifted from each other by an energy $2s$. We consider a generic dispersion $\epsilon(\mathbf{k}) = -2t[\cos(k_x) + \cos(k_y) + \cos(k_z)]$ with t being a hopping energy scale and focus on the limit $s/t \ll 1$ implying small but finite splitting between the corresponding two Fermi surfaces. To take into account the effect of SOC present in these materials, we phenomenologically consider a Rashba-type SOC. Note that although (Ta, Nb)OsSi are globally centrosymmetric, inversion symmetry is broken locally at the (Ta, Nb) sites due to the TiNiSi-type structure [25] which can result in a Rashba-type SOC [26, 27]. Then the normal state Hamiltonian for the toy model is, $\hat{H}_0 = \sum_{\mathbf{k}} \hat{c}_{\mathbf{k}}^{\dagger} \cdot H_0(\mathbf{k}) \cdot \hat{c}_{\mathbf{k}}$, defining $\hat{c}_{\mathbf{k}} = \begin{bmatrix} \tilde{c}_{\uparrow, \mathbf{k}} \\ \tilde{c}_{\downarrow, \mathbf{k}} \end{bmatrix}$ with $\tilde{c}_{p, \mathbf{k}} = \begin{bmatrix} c_{+, p, \mathbf{k}} \\ c_{-, p, \mathbf{k}} \end{bmatrix}$. $c_{\pm, p, \mathbf{k}}$ is an electron annihilation operator in the \pm band with spin $p = \uparrow$ and \downarrow , and

$$H_0(\mathbf{k}) = \sigma_0 \otimes \begin{bmatrix} \xi_{+}(\mathbf{k}) & 0 \\ 0 & \xi_{-}(\mathbf{k}) \end{bmatrix} + (k_y \sigma_x - k_x \sigma_y) \otimes \alpha \tau_x \quad (6)$$

where $\xi_{\pm}(\mathbf{k}) = \epsilon_{\pm}(\mathbf{k}) - \mu$ with μ being the chemical potential and σ_0 is the identity matrix in spin space. The second term in Eq. (6) is a Rashba-type inter-orbital SOC of strength α . Although, in general, both intra- and inter-orbital SOC terms should be present, we can fit the specific heat data well only in the limit of inter-orbital SOC strength much larger than the intra-orbital SOC strength, emphasizing the inter-orbital nature of the pairing in the INT state [17].

Using the Bogoliubov de-Gennes formalism [3], we computed the quasi-particle excitation spectrum for the toy model in the INT state considering the temperature dependence of $\Delta_a(T)$ in the form of Eq. (S.18). The specific heat is then computed using the temperature dependent quasi-particle spectrum to fit the experimentally measured electronic specific heat after subtracting the phonon contribution [17]. In the fitting shown in Fig. 4, we fixed $s/t \ll 1$ and T_c with the corresponding experimental values for (Ta, Nb)OsSi. Then there are only three fitting parameters: α/t , $\boldsymbol{\eta}$ and $\Delta_0/(k_B T_c)$ with $\Delta_0 \equiv \Delta_a(0)$. Fig. 4 shows that the electronic specific heat for both TaOsSi [28] and NbOsSi can be fitted very well with small SOC strengths ($\alpha/t \ll 1$) in the weak coupling limit. The corresponding INT ground state has $|\mathbf{q}| = 0.03$ implying small but finite spin polarization which leads to the spontaneous magnetization in the superconducting state seen in the ZF- μ SR experiments.

CONCLUSIONS

We have demonstrated through detailed μ SR measurements that (Ta, Nb)OsSi belong to the rare class of TRS-breaking superconductors represented by LaNiC₂, LaNiGa₂ and UTe₂, all of which have very low-symmetry crystal structures providing a unique opportunity to constrain the superconducting order parameter from symmetries. While LaNiC₂ [8] and LaNiGa₂ [10, 11] show two full gaps in the superconducting state arising from two spin channels, UTe₂ [14, 29] shows point nodes and two different transitions in the superconducting state and only below the lowest transition temperature does the TRS breaking occur. In contrast, (Ta,Nb)OsSi show TRS breaking at T_c but have a full gap and low temperature thermodynamic properties similar to a conventional BCS-type superconductor as evidenced from the TF- μ SR and the specific heat data. Similarly, it will be interesting to investigate the other known isostructural superconductors in this family for possible TRS-breaking superconducting ground states, e.g. ZrOsSi which has contrasting properties than (Ta,Nb)OsSi and comparatively low T_c [30], ZrIrSi and HfIrSi [15].

By symmetry analysis and model calculations, the phenomenology of the superconducting properties of (Ta,Nb)OsSi are found to be overall consistent with a nonunitary triplet superconducting ground state. The presence of the Dirac points close to the Fermi level promotes interband pairing and further justifies the applicability of a minimal two-band toy model to describe the low energy normal state properties [12]. The nonsymmorphic symmetries present in (Ta,Nb)OsSi can allow for nodes in the order parameter at the Brillouin zone boundaries resulting in nodal superconducting states which are clearly incompatible with the full gap observed in the experiments. However, the nonsymmorphic symmetries can lead to degeneracies in the Bogoliubov quasi-particle bands which can result in topological superconductivity [12]. Further experimental studies in these materials, such as high-resolution ARPES, are highly desirable to confirm the presence of the symmetry-protected Dirac points close to the Fermi level, when the single crystals of these materials become available. (Ta,Nb)OsSi are therefore special symmetry-protected 3D Dirac semimetal superconductors that provide promising material platforms to investigate the rich physics arising from an interplay between topological Dirac fermions and unconventional TRS-breaking superconductivity.

Acknowledgements: PKB gratefully acknowledges the ISIS Pulsed Neutron and Muon Source of the UK Science & Technology Facilities Council (STFC) for access to the muon beam times. SKG acknowledges the Leverhulme Trust for support through the Leverhulme

early career fellowship and thanks A. Agarwala, J. Quintanilla and T. Shiroka for discussions and comments on the manuscript. XX acknowledges the financial support from NSFC under Grant No. 11974061 and useful discussions with Xiangang Wan and Dong Qian.

Author contributions: S.K.G., P.K.B and X.X conceived and initiated the project. C.X. and X.X. grew and characterized the samples used in this study. P.K.B and A.D.H. conducted the muon spin rotation and relaxation experiments. B.L. and J.Z.Z performed the first-principles calculations. S.K.G constructed the theoretical understanding and wrote the paper with input from all the co-authors.

* Electronic address: S.Ghosh@kent.ac.uk

† These authors contributed equally: S. K. Ghosh and P. K. Biswas.

‡ Electronic address: adrian.hillier@stfc.ac.uk

§ Electronic address: xuxiaofeng@zjut.edu.cn

- [1] N. P. Armitage, E. J. Mele, and A. Vishwanath, Weyl and Dirac semimetals in three-dimensional solids, *Rev. Mod. Phys.* **90**, 015001 (2018).
- [2] B. Q. Lv, T. Qian, and H. Ding, Experimental perspective on three-dimensional topological semimetals, *Rev. Mod. Phys.* **93**, 025002 (2021).
- [3] S. K. Ghosh, M. Smidman, T. Shang, J. F. Annett, A. D. Hillier, J. Quintanilla, and H. Yuan, Recent progress on superconductors with time-reversal symmetry breaking, *J. Phys. Condens. Matter* **33**, 033001 (2020).
- [4] M. Sato and Y. Ando, Topological superconductors: a review, *Rep. Prog. Phys.* **80**, 076501 (2017).
- [5] J. F. Annett, Symmetry of the order parameter for high-temperature superconductivity, *Adv. Phys.* **39**, 83 (1990).
- [6] M. Sigrist and K. Ueda, Phenomenological theory of unconventional superconductivity, *Rev. Mod. Phys.* **63**, 239 (1991).
- [7] A. D. Hillier, J. Quintanilla, and R. Cywinski, Evidence for time-reversal symmetry breaking in the noncentrosymmetric superconductor LaNiC₂, *Phys. Rev. Lett.* **102**, 117007 (2009).
- [8] J. Chen, L. Jiao, J. Zhang, Y. Chen, L. Yang, M. Nicklas, F. Steglich, and H. Yuan, Evidence for two-gap superconductivity in the non-centrosymmetric compound LaNiC₂, *New J. Phys.* **15**, 053005 (2013).
- [9] A. D. Hillier, J. Quintanilla, B. Mazidian, J. F. Annett, and R. Cywinski, Nonunitary triplet pairing in the centrosymmetric superconductor LaNiGa₂, *Phys. Rev. Lett.* **109**, 097001 (2012).
- [10] Z. F. Weng, J. L. Zhang, M. Smidman, T. Shang, J. Quintanilla, J. F. Annett, M. Nicklas, G. M. Pang, L. Jiao, W. B. Jiang, Y. Chen, F. Steglich, and H. Q. Yuan, Two-gap superconductivity in LaNiGa₂ with nonunitary triplet pairing and even parity gap symmetry, *Phys. Rev. Lett.* **117**, 027001 (2016).
- [11] S. K. Ghosh, G. Csire, P. Whittlesea, J. F. Annett, M. Gradhand, B. Újfalussy, and J. Quintanilla, Quantita-

- tive theory of triplet pairing in the unconventional superconductor LaNiGa_2 , *Phys. Rev. B* **101**, 100506 (2020).
- [12] J. R. Badger, Y. Quan, M. C. Staab, S. Sumita, A. Rossi, K. P. Devlin, K. Neubauer, D. S. Shulman, J. C. Fetting, P. Klavins, *et al.*, Dirac lines and loop at the Fermi level in the time-reversal symmetry breaking superconductor LaNiGa_2 , *arXiv preprint arXiv:2109.06983* (2021).
- [13] S. Ran, C. Eckberg, Q.-P. Ding, Y. Furukawa, T. Metz, S. R. Saha, I.-L. Liu, M. Zic, H. Kim, J. Paglione, *et al.*, Nearly ferromagnetic spin-triplet superconductivity, *Science* **365**, 684 (2019).
- [14] T. Metz, S. Bae, S. Ran, I.-L. Liu, Y. S. Eo, W. T. Fuhrman, D. F. Agterberg, S. M. Anlage, N. P. Butch, and J. Paglione, Point-node gap structure of the spin-triplet superconductor UTe_2 , *Phys. Rev. B* **100**, 220504 (2019).
- [15] C. Benndorf, L. Heletta, G. Heymann, H. Huppertz, H. Eckert, and R. Pöttgen, NbOsSi and TaOsSi —two new superconducting ternary osmium silicides, *Solid State Sciences* **68**, 32 (2017).
- [16] E. Haque and M. A. Hossain, Elastic, electronic, thermodynamic and transport properties of XOsSi ($X = \text{Nb, Ta}$) superconductors: First-principles calculations, *J. Alloys and Compounds* **739**, 737 (2018).
- [17] See the Supplemental Material at xxx for details of the measurements of the crystal structure, heat capacity and critical field, as well as for the data analysis, DFT calculation, symmetry analysis and toy-model calculations.
- [18] R. Kubo, A stochastic theory of spin relaxation, *Hyperfine Interactions* **8**, 731 (1981).
- [19] J. E. Sonier, J. H. Brewer, and R. F. Kiefl, μSR studies of the vortex state in type-II superconductors, *Rev. Mod. Phys.* **72**, 769 (2000).
- [20] E. H. Brandt, Properties of the ideal Ginzburg-Landau vortex lattice, *Phys. Rev. B* **68**, 054506 (2003).
- [21] R. Prozorov and R. W. Giannetta, Magnetic penetration depth in unconventional superconductors, *Supercond. Sci. Tech.* **19**, R41 (2006).
- [22] A. Carrington and F. Manzano, Magnetic penetration depth of MgB_2 , *Physica C* **385**, 205 (2003).
- [23] C. Q. Xu, B. Li, J. J. Feng, W. H. Jiao, Y. K. Li, S. W. Liu, Y. X. Zhou, R. Sankar, N. D. Zhigadlo, H. B. Wang, Z. D. Han, B. Qian, W. Ye, W. Zhou, T. Shiroka, P. K. Biswas, X. Xu, and Z. X. Shi, Two-gap superconductivity and topological surface states in TaOsSi , *Phys. Rev. B* **100**, 134503 (2019).
- [24] The nonsymmorphic symmetries present in $(\text{Ta, Nb})\text{OsSi}$, in general, can give rise to superconducting order parameters with additional symmetry required nodes along the high symmetry directions in the Brillouin zone boundaries but cannot give rise to a multicomponent order parameter to facilitate TRS breaking [12, 31, 32].
- [25] K. Araki, T. Kohei, H. Tanaka, S. Nakamura, T. Nojima, A. Ochiai, and K. Katoh, Magnetic and transport properties of YbNiGe with a TiNiSi -type structure, *J. Phys. Soc. Jpn.* **88**, 114709 (2019).
- [26] S.-L. Wu, K. Sumida, K. Miyamoto, K. Taguchi, T. Yoshikawa, A. Kimura, Y. Ueda, M. Arita, M. Nagao, S. Watauchi, *et al.*, Direct evidence of hidden local spin polarization in a centrosymmetric superconductor $\text{LaO}_{0.55}\text{F}_{0.45}\text{BiS}_2$, *Nat. Commun.* **8**, 1 (2017).
- [27] X. Zhang, Q. Liu, J.-W. Luo, A. J. Freeman, and A. Zunger, Hidden spin polarization in inversion-symmetric bulk crystals, *Nat. Phys.* **10**, 387 (2014).
- [28] Although the experimental specific heat data for TaOsSi was shown to be fitted well by a two-gap model having more fitting parameters [23], we note from Fig. 4 that the two-band toy model in the INT ground state giving rise to a single full gap provides a very good fitting as well.
- [29] I. Hayes, D. Wei, T. Metz, J. Zhang, Y. Eo, S. Ran, S. Saha, J. Collini, N. Butch, D. Agterberg, *et al.*, Multicomponent superconducting order parameter in UTe_2 , *Science* **373**, 797 (2021).
- [30] W. X. Zhong, B. Chevalier, J. Etourneau, and P. Hagemuller, Relationships between occurrence of superconductivity and crystal structure in new equiatomic ternary silicides MTSi ($M = \text{Ti, Zr, Hf}$ and $T = \text{Ru, Os, Rh}$), *Solid State Communications* **59**, 839 (1986).
- [31] S. Sumita and Y. Yanase, Unconventional superconducting gap structure protected by space group symmetry, *Phys. Rev. B* **97**, 134512 (2018).
- [32] S. Sumita, T. Nomoto, K. Shiozaki, and Y. Yanase, Classification of topological crystalline superconducting nodes on high-symmetry lines: Point nodes, line nodes, and Bogoliubov Fermi surfaces, *Phys. Rev. B* **99**, 134513 (2019).
- [33] M. Tinkham, *Introduction to Superconductivity* (McGraw-Hill Inc., 1996).

Supplemental Material
for
“Time-Reversal Symmetry Breaking Superconductivity in Three-Dimensional Dirac Semimetallic Silicides”

Abstract: In this Supplemental Material, we present details of the synthesis, characterization measurements, experimental methods and data analysis for the (Ta, Nb)OsSi materials. We also give additional band structure results, details of the symmetry analysis and computation of the specific heat using the Bogoliubov de-Gennes formalism for a toy model in the INT state.

Synthesis and characterization of (Ta, Nb)OsSi samples

Polycrystalline TaOsSi and NbOsSi were synthesized by the arc-melting method [15, 23]. The room-temperature crystal structure was characterized by X-ray diffraction (XRD) equipped in a Rigaku diffractometer with Cu K- α radiation and a graphite monochromator (see Fig. S.1). The crystallographic parameters are listed in Table I for concreteness. Resistivity (the upper critical field, see Fig. S.2), heat capacity properties were measured using Quantum Design Physical Property Measurement System (QD-PPMS). The magnetic susceptibility was studied in Quantum Design Magnetic Property Measurement System (QD-MPMS). We note from Fig. S.2 that the zero temperature values of the upper critical fields for TaOsSi and NbOsSi are ≈ 4 T and 1.2 T respectively, both of which are much larger than the applied transverse fields in the TF- μ SR measurements.

TABLE I. Crystallographic lattice parameters obtained for TaOsSi and NbOsSi.

Material	$a(\text{\AA})$	$b(\text{\AA})$	$c(\text{\AA})$
TaOsSi	6.26(5)	3.89(3)	7.25(9)
NbOsSi	6.28(1)	3.89(7)	7.27(3)

TABLE II. Parameters related to the experimental specific heat data.

Material	T_c (K)	γ (mJ/mol - K ²)	β (mJ/mol - K ⁴)	δ (mJ/mol - K ⁶)
TaOsSi	5.6	7.90	0.044	0.0014
NbOsSi	3.2	14.15	0.950	0.0310

The heat capacity was measured in zero field using a Quantum Design Physical Property Measurement System (QD-PPMS) with a ³He insert to get down to 0.5 K. The total specific heat C_{tot} at low temperatures is made up of mainly two contributions,

$$C_{tot} = C_{el} + C_{ph} \quad (\text{S.1})$$

where C_{el} is the electronic specific heat having the form in the normal state

$$C_{el} = \gamma T \quad (\text{S.2})$$

with γ being the Sommerfeld coefficient, C_{ph} is the specific heat due to the phonons given by

$$C_{ph} = \beta T^3 + \delta T^5 \quad (\text{S.3})$$

with β and δ being temperature independent parameters. We define

$$C' = \gamma T + \beta T^3 + \delta T^5. \quad (\text{S.4})$$

We extract the electronic specific heat from the experimentally determined total specific heat by fitting the specific heat in the normal state with C' as shown in the Fig. S.3 and the corresponding parameters are shown in the Table II.

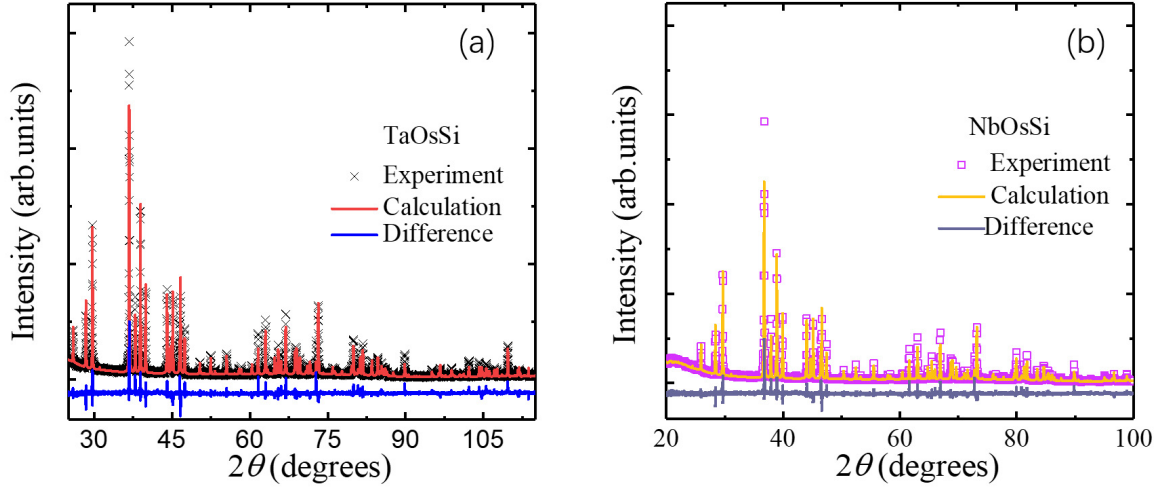


FIG. S.1. **XRD pattern.** Powder XRD pattern and Rietveld refinement for (a) TaOsSi and (b) NbOsSi.

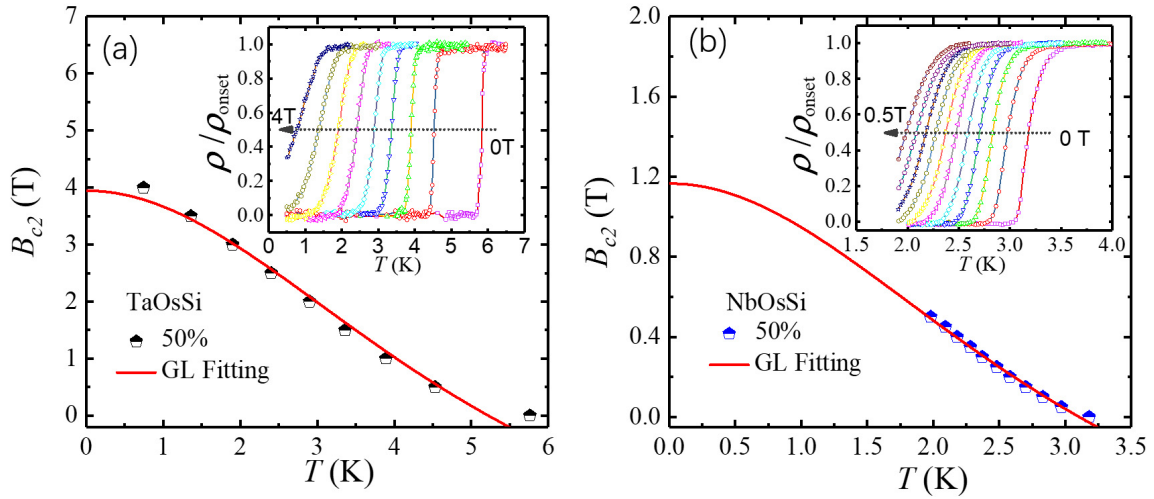


FIG. S.2. **Upper critical field.** Temperature dependence of the upper critical field B_{c2} , as determined by the 50% criteria at which the resistivity drops to 50% of its normal-state value ρ_{onset} just above T_c (illustrated in the insets) for (a) TaOsSi and (b) NbOsSi. Red solid lines represent the fits based on the Ginzburg-Landau (GL) theory.

Band structure

The crystal structure of (Ta,Nb)OsSi is centrosymmetric and orthorhombic. The space group Pnma (no. 62) is nonsymmorphic which has three glide mirror planes: $G_1 = \{m_{(0,1,0)}|t_{(0,1/2,0)}\}$, $G_2 = \{m_{(0,0,1)}|t_{(1/2,0,1/2)}\}$ and $G_3 = \{m_{(1,0,0)}|t_{(1/2,1/2,1/2)}\}$ where $m_{(\alpha,\beta,\gamma)}$ denotes reflection in the plane (α,β,γ) and t is a fractional translation parallel to the plane (α,β,γ) . Then we can define the composite anti-unitary symmetry operations $\Theta_i = G_i \star \mathcal{T}$ with

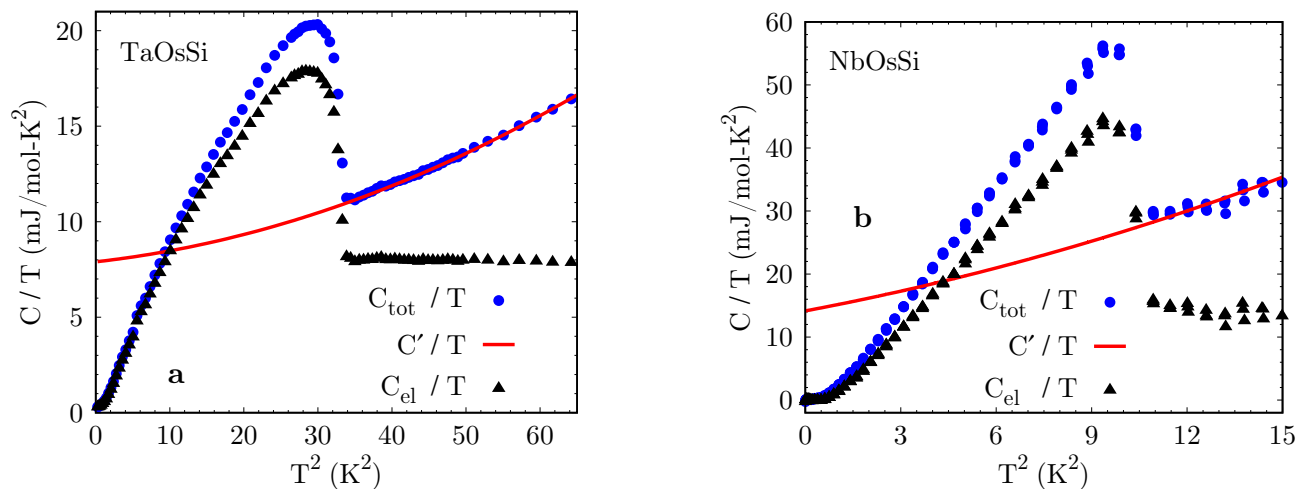


FIG. S.3. **Specific heat.** Experimental specific heat data for TaOsSi in **a** and for NbOsSi in **b**.

$i = 1, 2$ and 3 , and \mathcal{T} is the time-reversal operator, such that

$$\Theta_1(x, y, z, t) \longrightarrow (x, -y + \frac{1}{2}, z, -t) \quad (\text{S.5})$$

$$\Theta_2(x, y, z, t) \longrightarrow (x + \frac{1}{2}, y, -z + \frac{1}{2}, -t) \quad (\text{S.6})$$

$$\Theta_3(x, y, z, t) \longrightarrow (-x + \frac{1}{2}, y + \frac{1}{2}, z + \frac{1}{2}, -t) \quad (\text{S.7})$$

where (x, y, z) are the spatial coordinates along the a -, b - and c -axes in units of the corresponding lattice constants. Most importantly, $\Theta_1^2 = 1$, $\Theta_2^2 = e^{-ik_x a}$ and $\Theta_3^2 = e^{-i(k_y b + k_z c)}$. Then at the Brillouin zone boundary $k_x a = \pi$ we have $\Theta_2^2 = -1$ which leads to two-fold degeneracy of all eigenstates in this plane.

We have performed detailed band structure calculations of $A\text{OsSi}$ ($A = \text{Ta}$ and Nb) using density functional theory (DFT) within the generalized gradient approximation (GGA). The four Fermi surface sheets of NbOsSi (without SOC) are shown in Fig. S.4. The Fermi surface sheets shown in the panels (a), (b), (c) and (d) of Fig. S.4 contribute 8.1%, 45.1%, 37.6% and 9.2% respectively to the density of states at the Fermi level as seen from Fig. S.5a. We note from Fig. S.5b that the Nb $4d$ -orbitals and Os $5d$ -orbitals contribute the most to the density of states at the Fermi level.

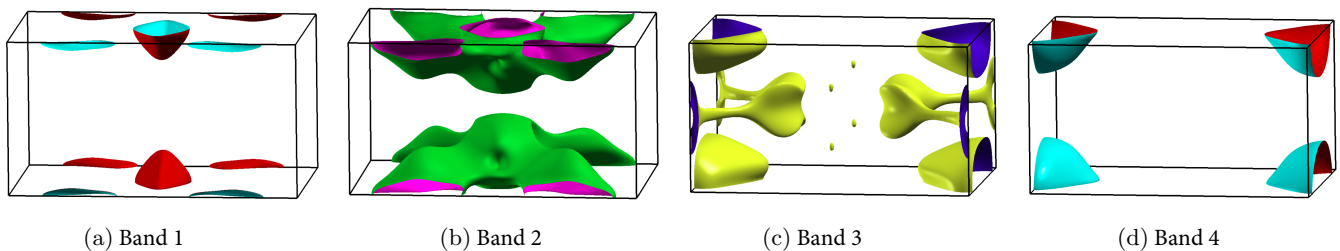


FIG. S.4. **Fermi surfaces of NbOsSi without SOC.** Panels (a)–(d) are from a side view of the four Fermi surface sheets of NbOsSi without SOC.

The coordinates of two of the Dirac points are listed in Table III for both TaOsSi and NbOsSi. The other two Dirac points are just time-reversal copies of these ones. The dispersions close to the Dirac points of NbOsSi are shown in Fig. S.6. Surface states on (100) and (001) planes for NbOsSi are shown in Fig. S.7a and b, where \bar{D} is the projection of Dirac point at $(0.50, 0.50, 0.16)$ on each plane.

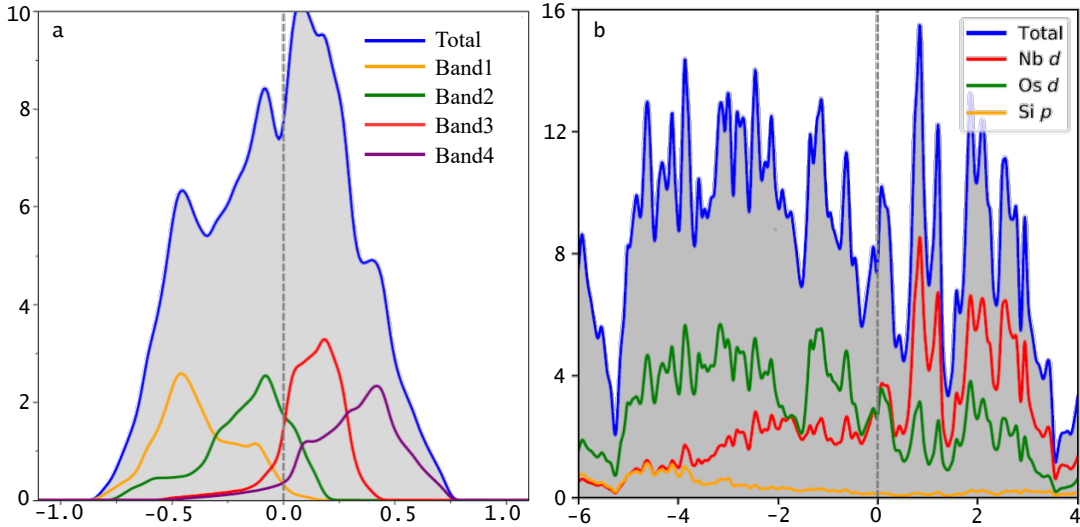


FIG. S.5. **Projected density of states for NbOsSi.** **a** Contribution of the four Fermi surfaces without SOC to the density of states for NbOsSi. **b** Contribution of the different orbitals of the different atoms to the density of states for NbOsSi.

TABLE III. Positions of Dirac points for TaOsSi and NbOsSi.

Material	$k_x(2\pi/a)$	$k_y(2\pi/b)$	$k_z(2\pi/c)$
TaOsSi	0.50	0.50	0.41
	0.50	0.48	0.30
NbOsSi	0.50	0.50	0.16
	0.50	0.48	0.10

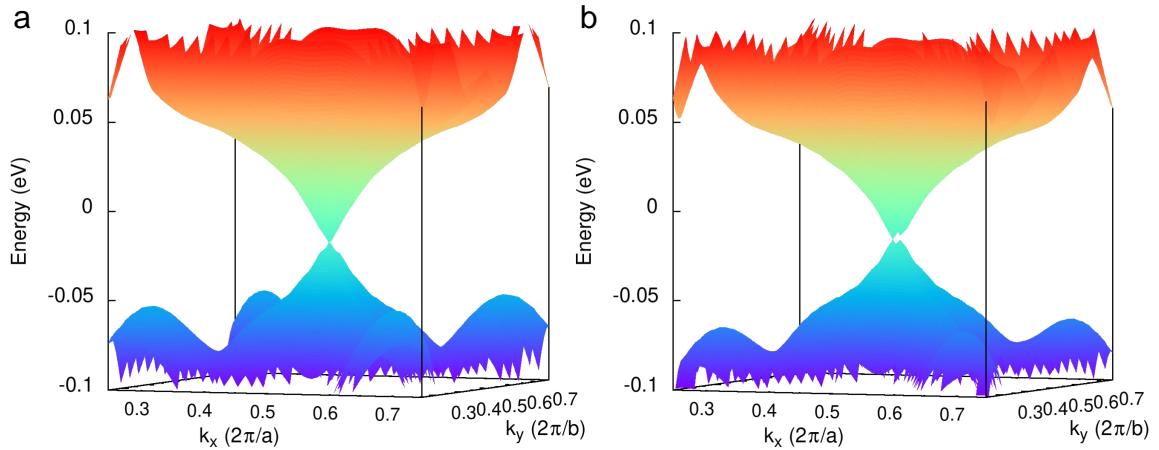


FIG. S.6. **Dirac points of NbOsSi.** The energy dispersions near the Dirac points given in Table III for NbOsSi with SOC are shown in the panels **a** and **b**.

Properties of the INT state for a two-band toy model

In this section, we describe the computation of the specific heat for a two-band toy model in the INT state [10, 11] using the Bogoliubov de-Gennes (BdG) formalism [3]. In the toy model, the two rigidly shifted energy bands, which can arise from two nearly degenerate effective orbitals, have the dispersions

$$\epsilon_{\pm}(\mathbf{k}) = \epsilon(\mathbf{k}) \pm s \quad (\text{S.8})$$

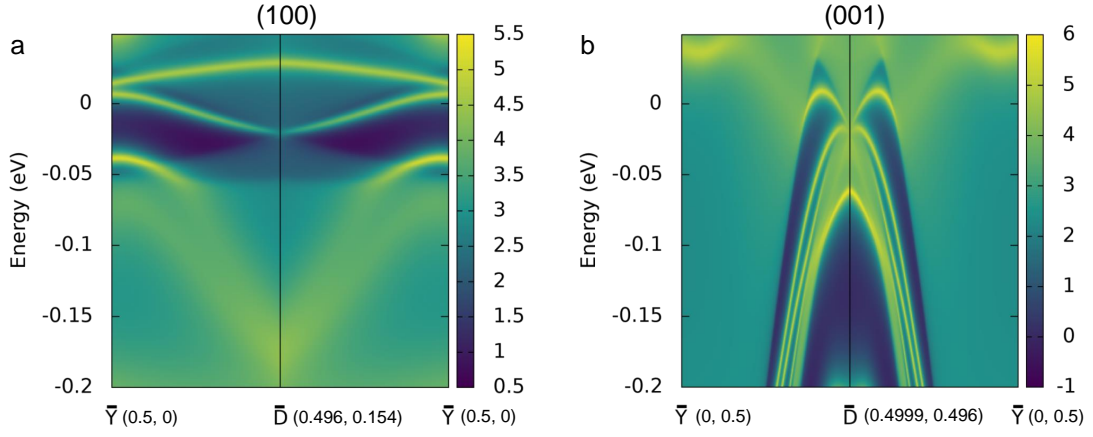


FIG. S.7. **Surface states.** Surface states on (100) and (001) planes for NbOsSi.

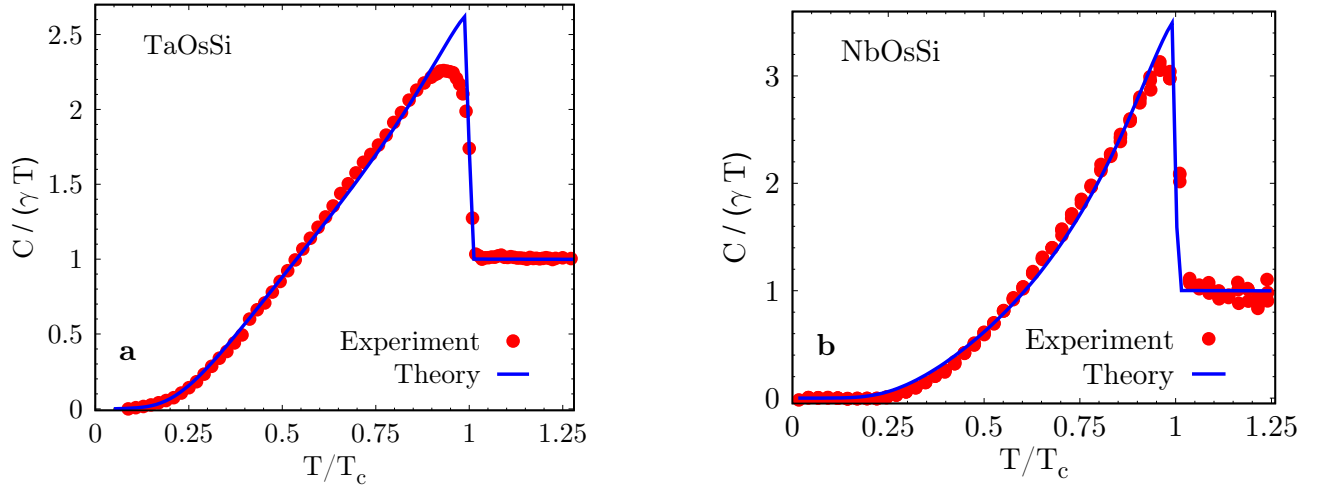


FIG. S.8. **Fitting the specific heat in the dominant interorbital SOC limit.** Fitting the experimental electronic specific heat data considering both the intraorbital and the interorbital spin-orbit coupling with $s/t = 0.1$, $\mu/t = -3.0$ and $\boldsymbol{\eta} = \frac{1}{\sqrt{3}}(1, e^{i\pi/100}, e^{i101\pi/100})$. **a)** TaOsSi case with parameters $\Delta_0/(k_B T_c) = 2.40$, $\alpha/t = 0.15$ and $\alpha_1/\alpha = 0.001$; and **b)** NbOsSi case with parameters $\Delta_0/(k_B T_c) = 3.4$, $\alpha/t = 0.20$ and $\alpha_1/\alpha = 0.001$.

where $\epsilon(\mathbf{k}) = -2t[\cos(k_x) + \cos(k_y) + \cos(k_z)]$ is a generic dispersion with t being a hopping parameter and s being the rigid energy shift, $s/t \ll 1$.

To take into account the effect of non-zero spin-orbit coupling (SOC), found in both the materials, in a simple way, we phenomenologically consider a Rashba-type SOC, which can arise due to the local inversion symmetry breaking [25–27] found in these materials. In general, we have both inter-orbital SOC of strength α and intra-orbital SOC of strength α_1 . Then the normal state Hamiltonian operator is

$$\hat{\mathcal{H}}_0 = \sum_{\mathbf{k}} \hat{c}_{\mathbf{k}}^\dagger \cdot H_0(\mathbf{k}) \cdot \hat{c}_{\mathbf{k}}, \quad (\text{S.9})$$

defining

$$\hat{c}_{\mathbf{k}} = \begin{bmatrix} \tilde{c}_{\uparrow, \mathbf{k}} \\ \tilde{c}_{\downarrow, \mathbf{k}} \end{bmatrix} \quad \text{with} \quad \tilde{c}_{p, \mathbf{k}} = \begin{bmatrix} c_{+, p, \mathbf{k}} \\ c_{-, p, \mathbf{k}} \end{bmatrix}. \quad (\text{S.10})$$

$c_{+, p, \mathbf{k}}$ is an electron annihilation operator in the \pm band with spin $p = \uparrow$ and \downarrow . The normal state Hamiltonian matrix is given by

$$H_0(\mathbf{k}) = \sigma_0 \otimes \begin{bmatrix} \xi_+(\mathbf{k}) & 0 \\ 0 & \xi_-(\mathbf{k}) \end{bmatrix} + (k_y \sigma_x - k_x \sigma_y) \otimes (\alpha \tau_x + \alpha_1 \tau_0) \quad (\text{S.11})$$

where $\xi_{\pm}(\mathbf{k}) = \epsilon_{\pm}(\mathbf{k}) - \mu$ with μ being the chemical potential and, σ_0 and τ_0 are the identity matrices in spin-space and orbital-space respectively.

The interaction part of the Hamiltonian in the INT channel [10, 11] is

$$\hat{\mathcal{H}}_I = \frac{1}{2} \sum_{\mathbf{k}} \left[\hat{c}_{\mathbf{k}}^{\dagger} \cdot \hat{\Delta} \cdot \hat{c}_{-\mathbf{k}}^{\dagger T} + \text{h.c.} \right] \quad (\text{S.12})$$

with the pairing potential in the INT state given by

$$\hat{\Delta} = \Delta_a (\boldsymbol{\eta} \cdot \vec{\sigma}) i \sigma_y \otimes i \tau_y, \quad (\text{S.13})$$

where Δ_a is the pairing amplitude. Then, the BdG Hamiltonian operator is

$$\begin{aligned} \hat{\mathcal{H}}_{\text{BdG}} &= \hat{\mathcal{H}}_0 + \hat{\mathcal{H}}_I \\ &= \frac{1}{2} \sum_{\mathbf{k}} \Psi_{\mathbf{k}}^{\dagger} H_{\text{BdG}}(\mathbf{k}) \Psi_{\mathbf{k}} + \text{constant} \end{aligned} \quad (\text{S.14})$$

with the Nambu operators defined as

$$\Psi_{\mathbf{k}} = \begin{bmatrix} \hat{c}_{\mathbf{k}} \\ \hat{c}_{-\mathbf{k}}^{\dagger T} \end{bmatrix} \quad (\text{S.15})$$

and the BdG Hamiltonian matrix is given by

$$H_{\text{BdG}}(\mathbf{k}) = \begin{bmatrix} H_0(\mathbf{k}) & \hat{\Delta} \\ \hat{\Delta}^{\dagger} & -H_0(-\mathbf{k})^T \end{bmatrix}. \quad (\text{S.16})$$

$H_{\text{BdG}}(\mathbf{k})$ is then diagonalized to obtain the Bogoliubov quasiparticle energy bands $E_n(\mathbf{k})$; $n = 1 \dots 4$ which are used to compute the specific heat using the formula [33]

$$C = \sum_{n, \mathbf{k}} \frac{1}{2} k_B \beta^2 \left\{ E_n(\mathbf{k}) + \beta \frac{\partial E_n(\mathbf{k})}{\partial \beta} \right\} E_n(\mathbf{k}) \text{sech}^2 [\beta E_n(\mathbf{k})/2] \quad (\text{S.17})$$

where $\beta = \frac{1}{k_B T}$ and k_B is the Boltzmann constant. The temperature dependence comes in the quasiparticle energy bands considering that the temperature dependence comes only from the pairing amplitude [22] as

$$\Delta_a(T) = \Delta_0 \tanh \left[1.82 \{1.018 (T_c/T - 1)\}^{0.51} \right] \quad (\text{S.18})$$

with $\Delta_a(0) \equiv \Delta_0$. We ignore any weak temperature dependence in the \mathbf{q} -vector.

To fit the specific heat data, we first fix the T_c of a particular material from experiments and then treat $\Delta_0/(k_B T_c)$, $\boldsymbol{\eta}$, α/t and α_1/α as fitting parameters. So, in general we have four fitting parameters. However, we can only fit the experimental specific heat data well in the limit $\alpha_1/\alpha \ll 1$, i. e. dominant interorbital SOC, without changing the topology of the resulting Fermi surfaces qualitatively. As seen from the example shown in Fig. S.8 in this limit we can fit the specific heat data for both the materials quite well in the weak coupling limit and a nonzero α_1 does not change the physics qualitatively as long as it is much smaller than α . Hence, we only consider the case $\alpha_1 = 0$ in the main text for simplicity.